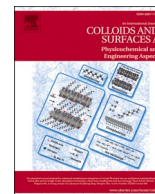




Contents lists available at ScienceDirect

Colloids and Surfaces A: Physicochemical and Engineering Aspects

journal homepage: www.elsevier.com/locate/colsurfa

Designing strategically functionalized hybrid porous polymers with octavinylsilsesquioxane/dibenzo[*g,p*]chrysene/benzo[*c*]-1,2,5-thiadiazole units for rapid removal of Rhodamine B dye from water

Ching-Wen Hsiao^{a,1}, Ahmed M. Elewa^{b,1}, Mohamed Gamal Mohamed^{a,c,*},
Mohammed G. Kotp^a, Mitch Ming-Chi Chou^a, Shiao-Wei Kuo^{a,d,*}

^a Department of Materials and Optoelectronic Science, Center of Crystal Research, National Sun Yat-Sen University, Kaohsiung 804, Taiwan

^b Department of Chemical Engineering, National Tsing Hua University, Hsinchu 300044, Taiwan

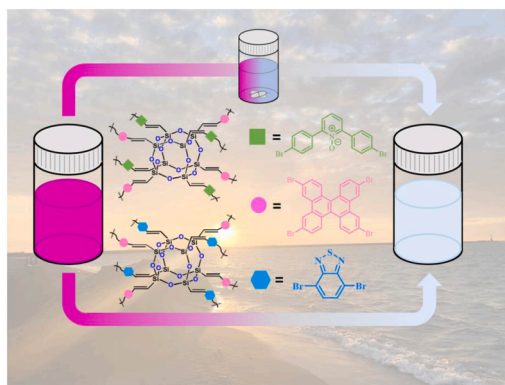
^c Chemistry Department, Faculty of Science, Assiut University, Assiut 71516, Egypt

^d Department of Medicinal and Applied Chemistry, Kaohsiung Medical University, Kaohsiung 807, Taiwan

HIGHLIGHTS

- The OVS-DBC-PO and OVS-DBC-BT POIPs were synthesized.
- The OVS-DBC-BT POIP exhibited a T_{d10} of 543 °C, char yield of 77 wt% and S_{BET} of 386 m² g⁻¹.
- The OVS-DBC-PO and OVS-DBC-BT POIPs provide an adsorption capacity of 65 and 66 mg g⁻¹.

GRAPHICAL ABSTRACT



ARTICLE INFO

Keywords:

Hybrid porous polymers
Octavinylsilsesquioxane
Dibenzo[*g,p*]chrysene
Benzo[*c*]-1,2,5-thiadiazole
Dye removal

ABSTRACT

Because of their large surface area and persistent pores that have exceptional adsorption capabilities, porous organic/inorganic polymers (POIPs) with octavinylsilsesquioxane (OVS) units have attracted much interest recently. In this study aimed at removing Rhodamine B (RhB) from wastewater, we utilized OVS nanoparticles synthesized through the Heck coupling process to produce two distinct types: OVS-DBC-PO and OVS-DBC-BT POIPs. OVS and a variety of chemical compounds containing Br, such as tetrabromodibenzo[*g,p*]chrysene (DBC-Br₄), 2,6-bis(4-bromophenyl)pyridine 1-oxide (PO-Br₂), and 4,7-dibromobenzo[*c*][1,2,5]thiadiazole (BT-Br₂) were involved in the reactions. Thermogravimetric analysis (TGA) results revealed that the high thermal decomposition temperature (T_{d10}) of OVS-DBC-PO and OVS-DBC-BT POIPs were 447 °C and 543 °C, respectively.

* Corresponding authors at: Department of Materials and Optoelectronic Science, Center of Crystal Research, National Sun Yat-Sen University, Kaohsiung 804, Taiwan.

E-mail addresses: mgamal.eldin12@yahoo.com, mgamal.eldin12@aun.edu.eg (M.G. Mohamed), kuosw@faculty.nsysu.edu.tw (S.-W. Kuo).

¹ These two authors contributed equally.

<https://doi.org/10.1016/j.colsurfa.2024.134658>

Received 7 May 2024; Received in revised form 16 June 2024; Accepted 28 June 2024

Available online 28 June 2024

0927-7757/© 2024 Elsevier B.V. All rights reserved, including those for text and data mining, AI training, and similar technologies.

Additionally, the OVS-POIPs demonstrated significant porosity, with the OVS-DBC-BT POIP exhibiting the highest specific BET surface area (S_{BET}) of $386 \text{ m}^2 \text{ g}^{-1}$. OVS-DBC-PO and OVS-DBC-BT POIPs exhibit exceptional porosity character. Based on dye adsorption measurements, RhB interacts with functional groups on the OVS-POIP samples' surface and penetrates their pores, enhancing the number of contact sites and the effectiveness of adsorption. Both OVS-DBC-PO and OVS-DBC-BT POIPs demonstrated maximum adsorption capacities of 65 and 66 mg g^{-1} , respectively, at a pH of 4 and a temperature of $25 \text{ }^\circ\text{C}$. As a result, OVS-DBC-PO and OVS-DBC-BT POIP materials could be viewed as efficient adsorbents for removing RhB from aqueous solutions and this study presents a novel way of making POIPs, which are adsorbents used in the filtration and treatment of water.

1. Introduction

Since the onset of the industrial era, the discharge of water pollution from factories has emerged as a pressing issue [1–3]. Illegal dumping of industrial and textile wastewater has escalated, presenting serious risks to human health and the environment [4–8]. The existence of dyes in bodies of water has sparked concerns regarding potential harm to various organisms, including humans [1–3]. Consequently, global attention has pivoted towards addressing the proper management of hazardous substances in wastewater. Alongside governmental policies integrating water management with human activities and ecosystem preservation, there's a growing focus on advancing wastewater treatment techniques. Methods such as membrane filtration, coagulation, ion exchange, adsorption, catalysis, sedimentation, and biodegradation are being explored as effective strategies to tackle this problem [9–11]. Among these, ion exchange and adsorption stand out for their simplicity, cost-effectiveness, and high efficiency in sewage treatment. Wastewater typically harbors numerous organic dyes, extensively utilized in industries ranging from textiles to pharmaceuticals, plastics, and paints. Discharging untreated toxic dye wastewater into aquatic environments remains a primary cause of environmental degradation [12].

Rhodamine B (RhB) stands out among numerous organic dyes for its high toxicity in textile wastewater, despite its widespread use in the textile sector owing to its good stability and resistance to biodegradation [13–19]. Not only does RhB pose a significant environmental threat, but

it also poses serious health risks to humans, classified as a carcinogenic and neurotoxic substance. Given these hazards, it's crucial to explore effective methods for eliminating Rhodamine B dye from water [13–20]. There are several traditional techniques for treating wastewater, such as aeration, coagulation, chemical flocculation, sedimentation, and filtration [9–11]. However, these techniques have drawbacks such as the generation of energy consumption, odors, and the need for extensive disposal areas. In recent years, several new dye removal methods have emerged, including electrochemical treatment, advanced oxidation processes (AOPs), adsorption, and biological treatment which are now commonly utilized. Among these, the adsorption method has gained significant traction for dye removal from wastewater [20–25]. In comparison to biotechnological approaches with their inherent limitations, adsorption stands out because of its great effectiveness, versatility, and affordability. Furthermore, the recent development of alginate, natural adsorbents, and porous organic polymers has introduced highly efficient organic sorbents to eliminate dyes from water solutions [26–36].

Because they may combine the benefits of both organic and inorganic materials, hybrid polymeric porous materials, or HPPs, have attracted a lot of interest. One significant type of 3D organic-inorganic hybrid nanosized compounds among them is cage-like organosilane [37–44]. These molecules, typically structured in the cubic $\text{R}_8\text{Si}_8\text{O}_{12}$ configuration, referred to as cage silsesquioxanes (SQs), have a silica-like core and substituents connected to each vertex of the cage [45–48]. SQs units have mechanical characteristics similar to inorganic

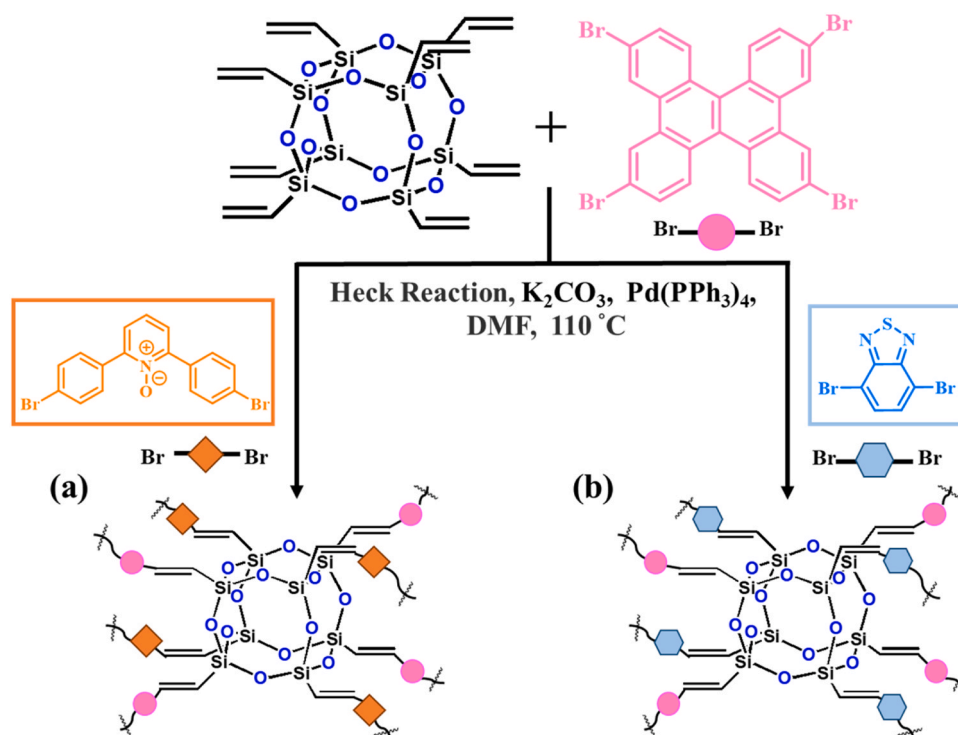


Fig. 1. Synthetic approach of (a) OVS-DBC-PO and (b) OVS-DBC-BT POIPs.

materials and great thermal stability [49–56]. Moreover, SQs offer the potential for further functionalization through organic methods. Among the various derivatives of caged sesquioxane, OVS stands out for its versatility. OVS could be utilized to produce porous materials through different synthesis routes, including the click reaction, hydrosilylation, Friedel-Crafts process, and Heck reaction [48,49,52]. The hybrid polymers synthesized using these methods retain the excellent optical and electrical properties of OVS. Porous organic polymers and OVS have gained increasing attention as adaptable building parts for fabricating porous materials due to their high stiffness and diverse functionality, offering numerous potential applications [48,49,52,57–62]. Notably, the Fu group successfully fabricated HPPs containing polyhedral oligomeric silsesquioxanes (POSS) with various sizes, such as T_8 , T_{10} , and T_{12} , for the removal of RhB [39]. Liu et al. [63] reported that HPP-3, containing OVS and TPE units, achieved adsorption capacities of 1666 mg g^{-1} for RB. Furthermore, the same researchers demonstrated that RhB could be removed by hybrid porous polymers (THPP) with an adsorption capacity of approximately 1402 mg g^{-1} [64]. Recently, our group reported the RhB adsorption capacities of OVS-TBN-THS HPP to be 42.12 mg g^{-1} , respectively [65]. DCB is a type of discotic DPAH and possesses a distinct helical configuration [66]. Due to their fascinating photophysical and electronic characteristics, such as extended excited state lifetimes and superior quantum yields, derivatives of dibenzo[*g,p*]chrysene have found applications in organic light-emitting diodes (OLEDs) [67], and various other fields in energy storage and H_2 production [68–70]. Benzothiadiazole (BT) commonly features π -bridges composed of benzene and thiophene rings [71–73]. In organic electronics, BT is widely used as an acceptor heterocycle. Identical configurations are referred to as BT rings with the same substituents at the 4 and 7 positions [74,75]. These structures are often utilized as monomers to create small molecules with diverse optoelectronic properties and donor-acceptor polymers [74,75].

Research on OVS-based POIP materials for water dye removal has been limited to date. Therefore, this study aims to utilize POIPs doped with OVS nanoparticles for rhodamine B elimination from wastewater. Two different POIPs were synthesized through the Heck coupling reaction, namely OVS-DCB-PO POIP and OVS-DCB-BT POIP. In these reactions, OVS with DBC- Br_4 /PO- Br_2 and DBC- Br_4 /BT- Br_2 were employed, using DMF as the solvent along with K_2CO_3 and $\text{Pd}(\text{PPh}_3)_4$ around 110°C for 3 days [Fig. 1]. The surface morphologies, porosity, and molecular chemical structures of both OVS- POIPs were thoroughly studied and determined using SEM, solid-state NMR [including ^{13}C and ^{29}Si and ^{13}C NMR], and BET. OVS-DCB-PO and OVS-DCB-BT POIPs were found to have a char yield of 77 wt% and a T_{d10} value of 447 and 543°C , respectively, based on the TGA results. Both OVS-DCB-PO and OVS-DCB-BT POIPs exhibited maximum capacity for adsorption of 65 and 66 mg g^{-1} , respectively. The dye results revealed that RhB not only interacts with the functional group on the surface of OVS-POIP samples but also permeates into their pores, thereby increasing the number of contact sites and improving adsorption effectiveness.

2. Experimental section

2.1. Materials

Nitromethane (CH_3NO_2), $\text{Pd}(\text{PPh}_3)_4$ (99 %), octavinylsilsesquioxane (OVS), 2,6-dibromopyridine N-oxide (PO), 2,1,3-benzothiadiazole (BT), 4-bromophenylboronic acid ($\text{Ph-BrB}(\text{OH})_2$), HBr solution (48 %), iron (III) chloride (FeCl_3), potassium carbonate (K_2CO_3 , 99 %), Br_2 (99.5 %), and AcOH (99.7 %), were purchased from Sigma–Aldrich.

2.2. Synthesis of PO- Br_2

In a nitrogen environment, a mixture of PO (1.3 g), $\text{Ph-BrB}(\text{OH})_2$ (4.13 g), K_2CO_3 (5.69 g), and $\text{Pd}(\text{PPh}_3)_4$ (0.3 mg) was placed into a flask. Then, THF (65 mL) and water (26 mL) were used as solvents. The

reaction temperature was maintained at 75°C and stirred for 2 days. Several filtration stages were conducted using water and methanol to remove excess monomer. The collected PO- Br_2 powder appeared white [Scheme S1]. FTIR analysis showed peaks at 3097 (C-H aromatic), 1517 , and 651 cm^{-1} . In the ^1H NMR spectrum [Figure S1], peaks were observed at 7.4, 7.8, and 7.9 ppm. In the ^{13}C NMR spectrum [Figure S2], peaks were observed in the range of 123–129, 132, and 148 ppm.

2.3. Synthesis of BT- Br_2

158 g of Br_2 solution and HBr (240 mL, 48 %) were mixed with BT (30 g). The resultant mixture was refluxed up to 90°C . This solution was added to a 0°C NaOH solution. The combination was then processed with DCM, resulting in a white powder (7.5 g, Scheme S2). ^1H NMR: 7.75 ppm [Figure S3]. ^{13}C NMR: 154–115 ppm [Figure S4].

2.4. Synthesis of DBC- Br_4

Under an N_2 atmosphere, 40 mL of dry DCM and 1.0 g of TPE- Br_4 (1.54 mmol) were combined. Subsequently, a solution of FeCl_3 (27.2 mmol) in 20 mL CH_3NO_2 was introduced into the reaction mixture using a septum. The resulting liquid was refluxed for 24 h. The product, DBC- Br_4 solid, appeared yellow solid in MeOH solution (0.81 g, yield: 81 %) [Scheme S3]. FTIR analysis revealed peaks at 3078, 1594 (C=C), and 591 cm^{-1} . In the ^1H NMR spectrum [Figure S5], peaks were observed at 7.77, 8.42, and 8.73 ppm.

2.5. Synthesis of OVS-DCB-PO and OVS-DCB-BT POIPs

TBN- Br_4 (0.015 g), OVS (0.5 g), PO- Br_2 (0.88 g), K_2CO_3 (1.75 g), and $\text{Pd}(\text{PPh}_3)_4$ (49.33 mg) in DMF (20 mL) were combined, mixed and heated 110°C for 3 days under a N_2 environment. After three days of reaction. After that, the solution cooled to 25°C . The solid was separated by several filtration stages using washing agents such as H_2O , MeOH, THF, and acetone. The resulting OVS-TBN-PO POIP formed a cream powder that could be isolated during purification. The synthesis method for OVS-DCB-BT POIP is identical to that of the previously mentioned OVS-DCB-PO POIP, with the exception that PO- Br_2 is substituted with BT- Br_2 . The resulting OVS-DCB-BT POIP formed a cream powder that could be isolated during purification. FTIR analysis showed peaks at 1607 and 3063 cm^{-1} .

3. Results and discussion

3.1. Synthesis and characterization of OVS-DCB-PO and OVS-DCB-BT POIPs

The synthesis of two distinct POIPs, namely OVS-DCB-PO and OVS-DCB-BT POIPs, involved the preparation of structural unit monomers, including PO- Br_2 , BT- Br_2 , and DBC- Br_4 . PO- Br_2 was synthesized by reacting the PO monomer with $\text{Ph-BrB}(\text{OH})_2$ in THF/water solution, resulting in a white powder [Scheme S1]. BT- Br_2 was obtained as a light-yellow powder from the BT monomer, HBr, and an excess of Br_2 solution [Scheme S2]. TPE- Br_4 was reacted with $\text{FeCl}_3/\text{CH}_3\text{NO}_2/\text{DCM}$ to create DBC- Br_4 , which is a white powder [Scheme S3]. In Figs. 1(a) and 1(b), the synthesis of OVS-DCB-PO and OVS-DCB-BT POIPs involved the Heck coupling reaction. These reactions utilized OVS, DBC- Br_4 /PO- Br_2 , and DBC- Br_4 /BT- Br_2 as the initial materials. As depicted in Fig. 1, the Heck coupling reaction occurred in DMF at 110°C , with $\text{Pd}(\text{PPh}_3)_4$ and K_2CO_3 serving as catalysts. Spectroscopic analyses were performed on DBC- Br_4 , PO- Br_2 , and BT- Br_2 compounds, including NMR and FTIR. Figures S1 and S2 display the recorded ^1H and ^{13}C NMR spectra of PO- Br_2 , while Figures S3 and S4 show those of BT- Br_2 (measured in $\text{DMSO-}d_6$). Clear peaks were observed for the chemical transitions of 7.93, 7.66, and 6.54 ppm in the ^1H NMR spectra of PO- Br_2 due to the aromatic ring's protons (Figure S1). This analysis was corroborated by the ^{13}C NMR

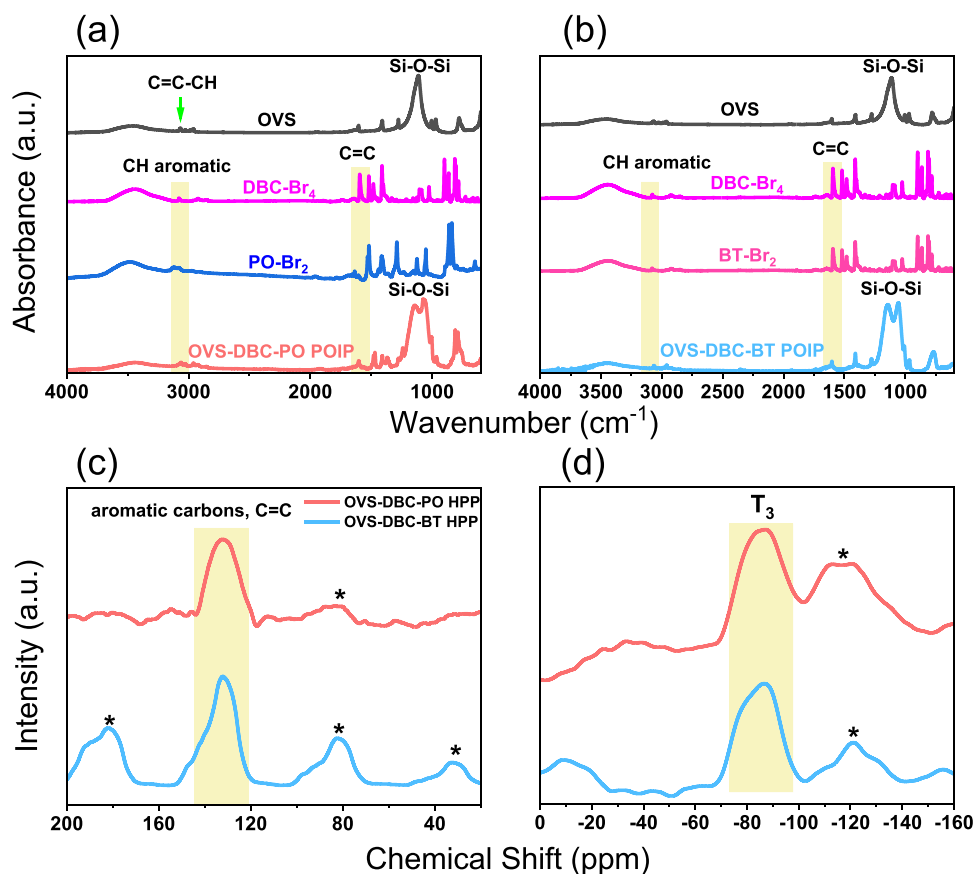


Fig. 2. FTIR profiles of (a) OVS, DBC-Br₄, PO-Br₂, and OVS-DBC-PO POIP, (b) FTIR profiles of OVS, DBC-Br₄, BT-Br₂, and OVS-DBC-BT POIP, (c) Solid-state ¹³C CP/MAS NMR and (d) ²⁹Si MAS NMR spectra of OVS-DBC-PO, and OVS-DBC-BT POIPs.

spectrum depicted in Figure S2, which displayed notable signals for aromatic rings at 148.4, 140.3, 131.8, 126.7, and 122.0 ppm. Similarly, in the ¹H NMR spectrum of BT-Br₂ (Figure S3), a proton's signal is at 7.7 ppm. In contrast, the ¹³C NMR spectrum (Figure S4) exhibited three clear peaks at 153.9, 132.6, and 153.9 ppm, corresponding to carbon atoms in the aromatic ring. The peaks observed at 7.77, 8.42, and 8.73 ppm in the ¹H NMR spectrum of DBC-Br₄ [Figure S5] correspond to the aromatic rings.

Fig. 2(a) displays the OVS's FTIR spectrum revealing clear

absorption peaks. The absorption peak of the Si-O-Si group is identified at 1108 cm⁻¹, the C=C absorption peak is observed at 1600 cm⁻¹, and the absorption peak for the C=C-H unit is situated at 3065 cm⁻¹. Furthermore, the FTIR spectrum of DBC-Br₄ (Fig. 2(a)) exhibits characteristic peaks for the C=C unit (1596 cm⁻¹). The C=C stretching vibration is prominent at 1517–1578 cm⁻¹ for PO-Br₂ and BT-Br₂ (Figs. 2 (a) and 2(b), respectively). After the Heck reaction, the Si-O-Si signal of OVS initially positioned at 1100 cm⁻¹ undergoes broadening, showing that a cross-linked network is developing to create OVS-DBC-PO and

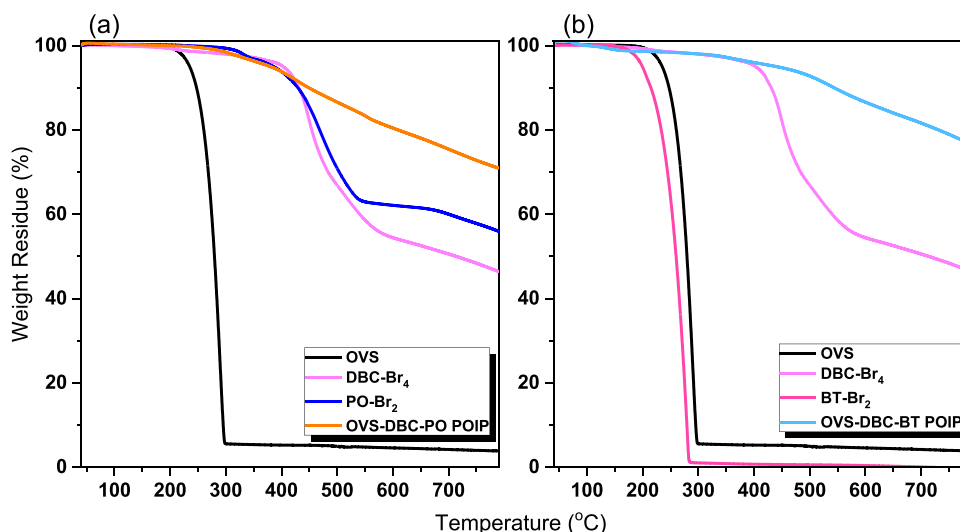


Fig. 3. TGA profiles of (a) OVS, DBC-Br₄, PO-Br₂, and OVS-DBC-PO POIP, and (b) OVS, DBC-Br₄, BT-Br₂ and OVS-DBC-BT POIP.

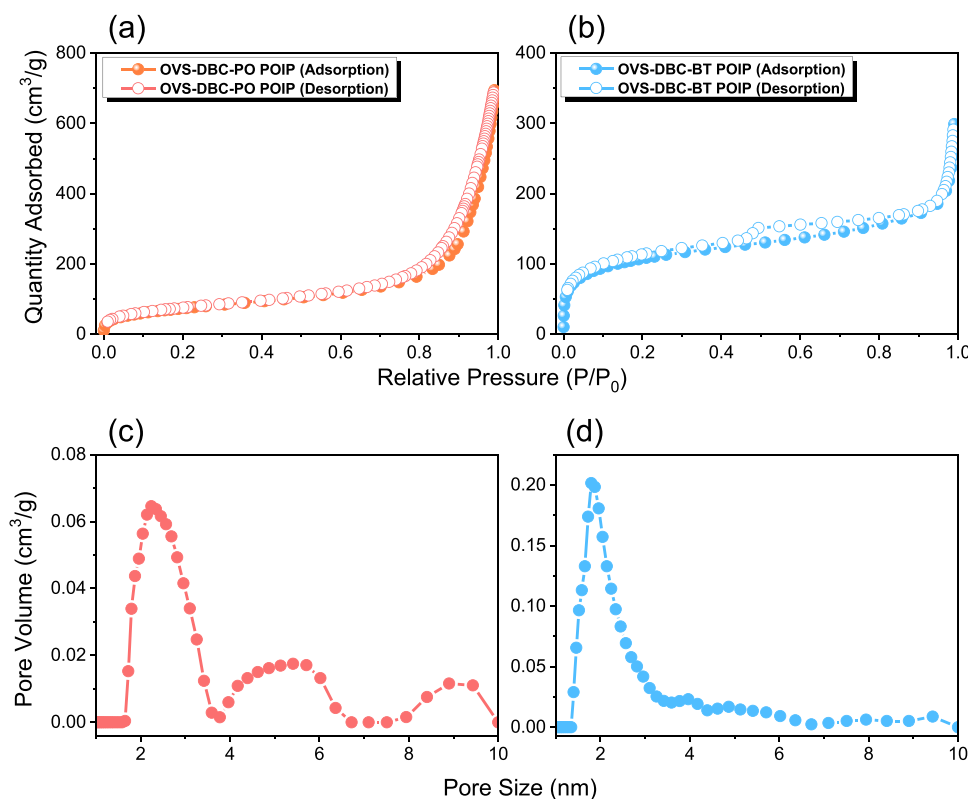


Fig. 4. (a-b) N₂ adsorption and desorption and (c-d) pore size profiles of OVS-DBC-PO (a, c), and OVS-DBC-BT POIPs (b, d).

OVS-DBC-BT POIPs framework. Additionally, the OVS-POIPs's FTIR spectra (Figs. 2(a) and 2(b)) show absorption bands for C=C stretching vibration in the region of 1580–1560 cm⁻¹, and for C=C-H, the absorption band is in the range of 3065–3070 cm⁻¹. Solid-state NMR was utilized to determine the structure of OVS following the Heck reaction. In Fig. 2(c), the ¹³C solid-state NMR spectra of OVS-DBC-PO and OVS-DBC-BT POIPs display signals for the aromatic units in the range of 150–125 ppm. The OVS cage in OVS-DBC-PO and OVS-DBC-BT POIPs was further confirmed using ²⁹Si NMR as shown in Fig. 2(d). No T₂ signal was observed in the ²⁹Si NMR, indicating that the OVS cage remained intact after the synthesis reaction and did not collapse. Based on these results, the successful formation of OVS-PO and OVS-BT POIPs is confirmed through spectral analysis.

The thermal properties of OVS, PO-Br₂, BT-Br₂, DBC-Br₄, OVS-DBC-PO, and OVS-DBC-BT POIPs were analyzed through TGA measurements [Figs. 3(a) and 3(b)]. It is evident from the curves that after the Heck coupling reaction, the thermal stability of the two HPPs is higher compared to their corresponding monomers [OVS, DBC-Br₄, PO-Br₂, and BT-Br₂]. Because of the internal cross-linked structure that was created during the reaction, thermal stability has increased. Among these two POIP structures, OVS-DBC-BT POIP exhibits the largest thermal stability. T_{d5} and T_{d10} were measured at 438 °C and 543 °C, respectively. The thermal behavior for OVS, PO-Br₂, BT-Br₂, DBC-Br₄, OVS-DBC-PO, and OVS-DBC-BT POIPs were summarized in Table S1.

The porosity of OVS-DBC-PO and OVS-DBC-BT POIPs was evaluated through N₂ adsorption and desorption at 77 K and the Brunauer-Emmett-Teller (BET) theory was used to transform the original data. The rapid adsorption of both OVS-POIPs at low and high P/P₀ values indicates the predominance of micropores and mesoporous, as illustrated in Figs. 4(a) and 4(b). According to the IUPAC categorization of adsorption isotherms, OVS-DBC-PO and OVS-DBC-BT POIPs are classified as Type I and Type IV, respectively. OVS-DBC-BT POIPs exhibit a higher specific BET surface area (386 m² g⁻¹) compared to OVS-DBC-PO POIPs (265 m² g⁻¹) [Figures S6, S7, and Table S2]. The predicted total

pore volumes (V_{total}) of OVS-DBC-PO and OVS-DBC-BT POIPs are 0.45 and 1.06 cm⁻³ g⁻¹, respectively. Figs. 4(c) and 4(d) reveal that the pore size diameters of OVS-DBC-PO and OVS-DBC-BT POIPs are 2.30 and 1.90 nm, respectively [using the nonlocal density functional theory (NLDFT) approach], demonstrating that the pores are predominantly microporous in both OVS-POIP materials. These findings prove that building OVS-based POIPs via the Heck coupling process is feasible.

To confirm the morphological features of OVS-DBC-PO and OVS-DBC-BT POIPs, HR-TEM and FE-SEM imaging techniques were employed. Fig. 5(a-d) present FE-SEM images of OVS-DBC-PO and OVS-DBC-BT POIPs, displaying aggregated spherical particles. In HR-TEM images, partially ordered porosity is observed for both OVS-POIPs, suggesting an organized configuration with organic linkers, as demonstrated in Fig. 5(e-i).

The elemental mapping depicted in Fig. 6 and S8 illustrates a consistent distribution of elements. It confirms the existence of C, N, O, and Si in OVS-TBN-PO POIP [Figure S8] and C, N, O, S, and Si in OVS-TBN-BT POIP [Fig. 6].

XPS scans were conducted to determine the relative chemical compositions and electronic states of carbon, nitrogen, oxygen, silica, and sulfur on the surface of the POIP materials. High-resolution XPS spectra plots for C1s, N1s, O1s, Si2p, and S2p for the two POIP samples are shown in Figure S9. The deconvoluted C1s spectra of OVS-DBC-PO and OVS-DBC-BT POIPs reveal four distinct peaks. The fitting results for these C1s spectra [Figure S9(a)] identify four types of carbon states in both OVS-DBC-PO and OVS-DBC-BT POIPs: sp² carbons bonded to oxygen (C-O, 286.55 eV), sp² carbons bonded to nitrogen (C-N, 285.50 eV), carbon atoms bonded to other carbon atoms (C=C, 284.90 eV), and carbons bonded to silicon atoms (C-Si, 284.23 eV). It has been reported that the C1s state cannot precisely distinguish between C-O and C-S due to their similar binding energies. Quantitatively, there is an observed increase in the C-O band percentage in OVS-DBC-BT POIP compared to OVS-DBC-PO POIP, which may suggest the inclusion of S-C in the BT ring of the former [Table S3]. Additionally, the

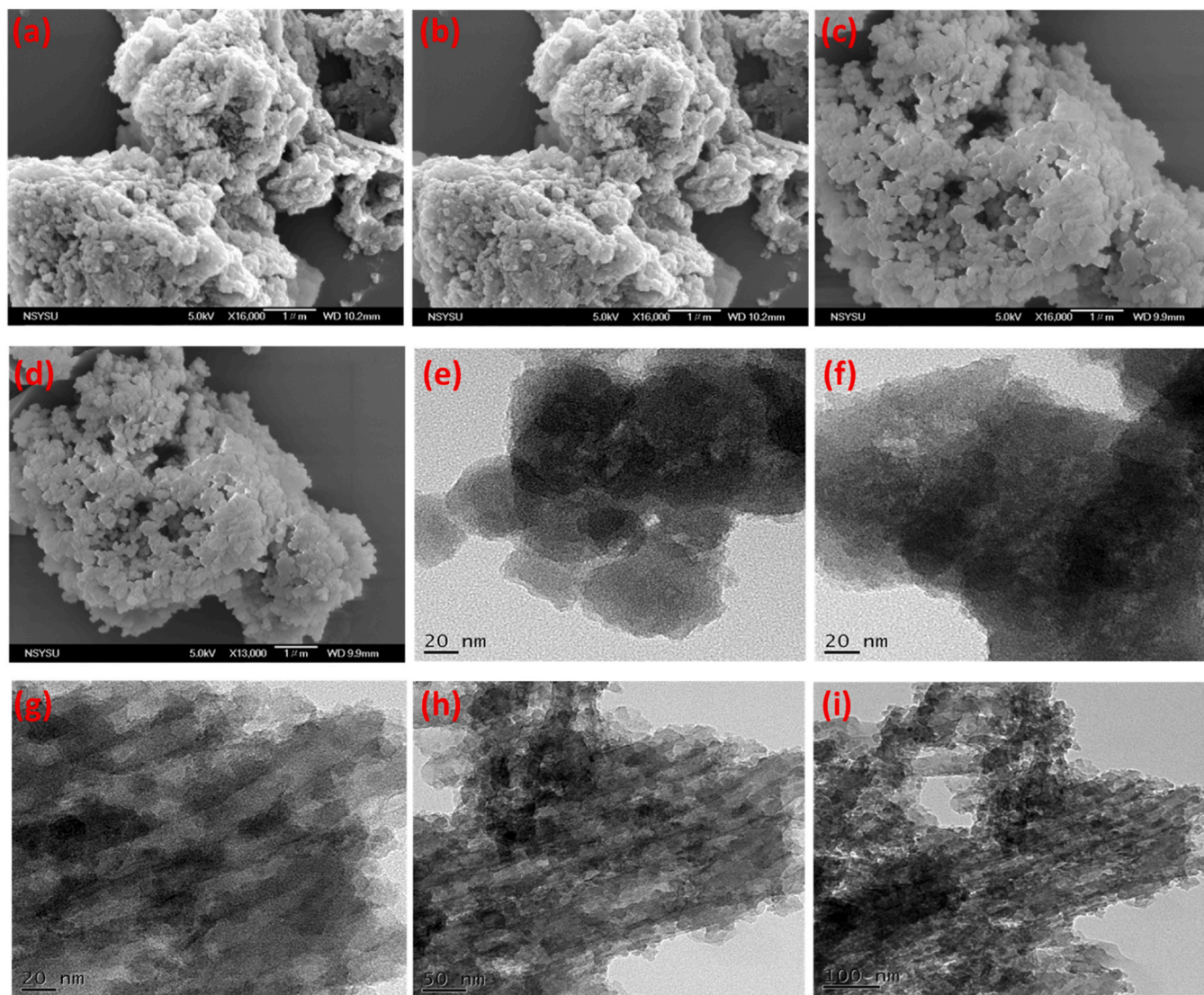


Fig. 5. . (a-d) SEM and (e-i) TEM images of (a, b, e, f) OVS-DBC-PO, and (c, d, g, h, i) OVS-DBC-BT POIPs.

deconvolution of the N1s spectra for OVS-DBC-PO and OVS-DBC-BT POIPs reveals the presence of two nitrogen forms in each POIP [Figure S9(b)]. For OVS-DBC-PO POIP, the N1s spectra deconvolutes at approximately 402.94 eV and 399.32 eV, corresponding to incorporated N-O and sp^2 -nitrogen bonded to carbon atoms (N-C), respectively (In contrast, the N1s spectra for OVS-DBC-BT POIP deconvolutes at approximately 400.28 eV and 399.32 eV, corresponding to incorporated N-S and sp^2 -nitrogen bonded to carbon atoms (N-C), respectively. Furthermore, the surfaces of both POIPs exhibit three types of oxygen states [Fig. 9(c)] located at 534.21 eV, 533.02 eV, and 532.05 eV, which can be attributed to oxygen atoms in O-H, O-C, or O-N, and Si-O, respectively. Notably, the presence of nitrogen in our POIPs can induce structural defects in unsaturated carbons at carbon edges. These defects are highly reactive with physically absorbed oxygen, forming oxygen-containing groups when exposed to air, as we have shown above. These oxygen species are in addition to those originating from the OVS moiety. Furthermore, the deconvolution of the XPS signal for the Si atom within OVS-DBC-PO and OVS-DBC-BT POIPs reveals three Si2p states: Si-O at 104.76 eV, Si-OH at 103.64 eV, and Si-C at 102.66 eV [Figure S9(d)]. Importantly, the high-resolution XPS of the OVS-DBC-BT POIP shows the S2p state at 167.36 eV [Figure S9(e)], which originates from the N-S-N incorporated in the BT ring.

3.2. The adsorption of RhB dye using OVS-DBC-PO and OVS-DBC-BT POIPs

Based on prior literature, RhB exists in three different protonated variants with varying charges: $RhBH^+$, $RhBH_2^{2+}$, and the zwitterion (RhB^\pm), appearing at different pH values. $RhBH_2^{2+}$ predominates at pH values below one, $RhBH^+$ is more common between pH 1 and 3, and RhB^\pm dominates at pH values greater than 4. Additionally, RhB molecules can combine to form dimers, with the degree of dimerization varying depending on the protonation forms; RhB^\pm exhibits a greater propensity for dimerization compared to positively charged cations. The degree of adsorption effectiveness is strongly influenced by the pH of the solution. In this work, we examined the POIPs' adsorption impact in solutions ranging in pH from 2 to 7. The results shown in Fig. 7 show that the synthesized OVS-DBC-PO and OVS-DBC-BT POIPs' RhB removal effectiveness is significantly influenced by the pH value of the solution. Both POIPs achieve a 100 % removal rate when the pH ranges from 2 to 4. However, as the pH increases, the removal rate gradually decreases. The observed trend is attributed to differences in the carbon material's surface charge and the structural changes induced by varying pH levels on distinct ionic species.

RhB ions carry a positive charge and remain as monomeric molecules at pH levels below 4, enhancing their ability to permeate the pore

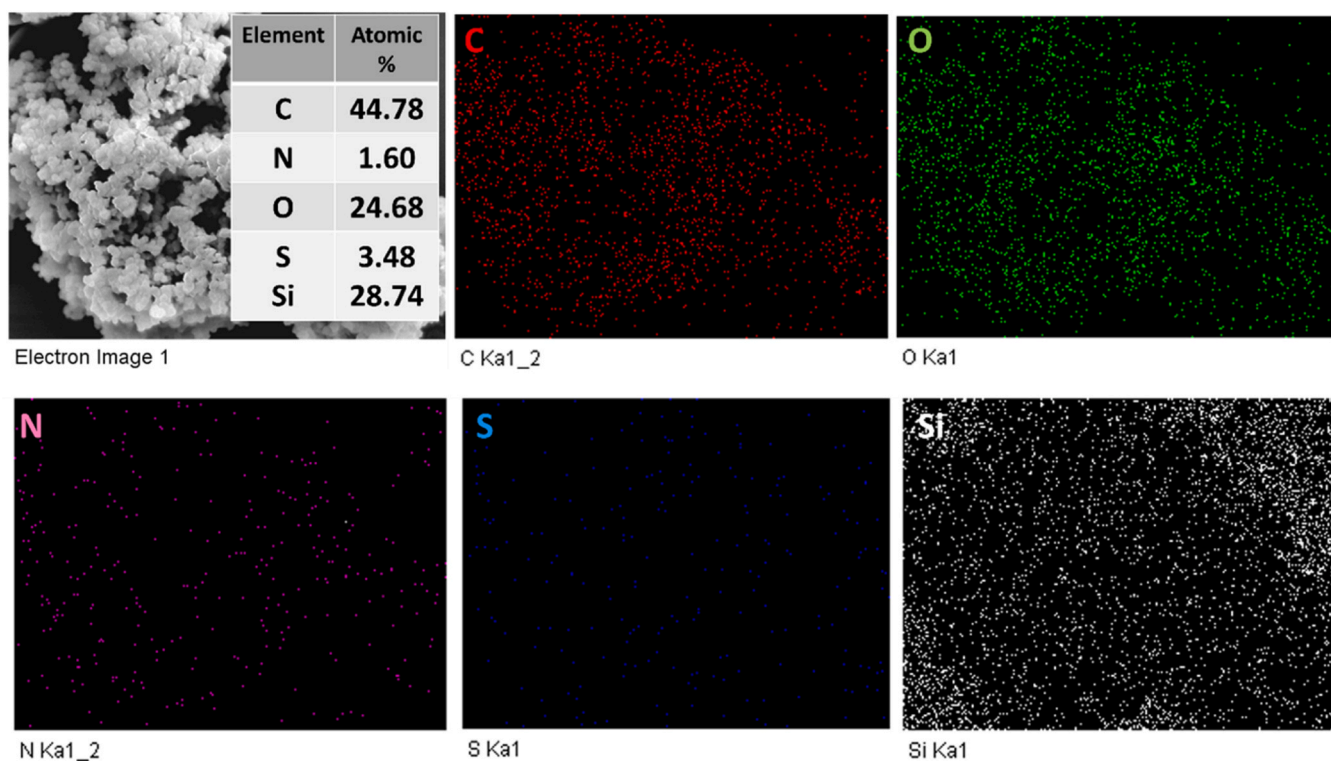


Fig. 6. SEM-EDS analyses [C, O, N, S, and Si atoms] in the OVS-DBC-BT POIP framework.

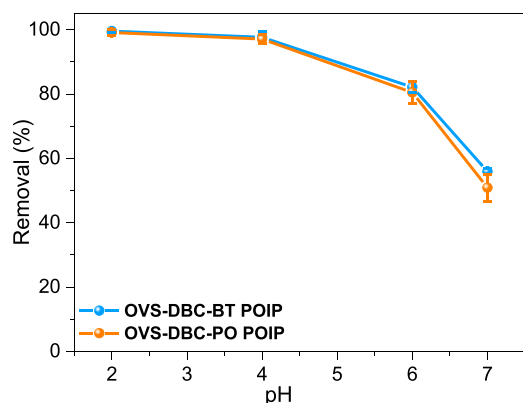


Fig. 7. Illustrates the impact of the initial pH of the solution on the adsorption process of RhB onto OVS-DBC-PO and OVS-DBC-BT POIPs. Dye concentration = 25 ppm; adsorbent mass = 0.5 g/L; contact time = 24 h.

structure of adsorbent materials. As the pH exceeds 4, RhB molecules aggregate and transition into a zwitterionic state, resulting in the development of bigger molecules known as dimers [76,77]. These macromolecular dimers are challenging to enter the pores due to their size, resulting in decreased adsorption efficiency. The efficiency of the adsorbent decreases with increasing pH, but at pH 7, the removal rate of OVS-DBC-BT POIP (57.0 %) is higher than that of OVS-DBC-PO POIP (46.5 %). This is attributed to the higher surface area of OVS-DBC-BT POIP compared to OVS-DBC-PO POIP, resulting in a relatively higher removal rate. OVS-DBC-BT POIP demonstrates excellent performance in RhB removal across various pH values. The zero-potential charges of OVS-DBC-PO and OVS-DBC-BT POIPs are 6.37 and 6.52, respectively [Figure S10]. The surfaces of the sorbents were negatively charged at a pH range of 2–5, resulting in electrostatic attraction between the sorbents and RhB in solution, which favored RhB capture. At pH levels higher than 7, the zeta potential of the sorbents' surfaces was positive,

indicating that the sorbents carried a positive charge. Consequently, physical π - π stacking attraction occurred between the sorbents and RhB dyestuff in the aqueous solution, contributing to RhB adsorption. Notably, at higher pH values, the adsorption capacities of RhB dyestuff using OVS-DBC-PO and OVS-DBC-BT POIPs decreased due to the conversion of cationic RhB dyestuff into its zwitterion form (RhB^{\pm}), which supports electrostatic repulsion. Thus, we can infer that electrostatic interaction plays a significant role in the adsorption of RhB dyestuff by OVS-DBC-PO and OVS-DBC-BT POIPs. Optimizing contact time is crucial to guarantee the whole equilibrium of the dye-adsorbent system in adsorption experiments. The superior adsorption effect of OVS-DBC-BT POIP compared to OVS-DBC-PO POIP could be attributed to the former's higher specific surface area. To confirm the efficiency of the materials in the adsorption process, the removal of RhB by the two OVS-POIP at different contact times was evaluated, as shown in Figs. 8(a) and 8(b). Fig. 8(b) illustrates the effect of interaction duration on RhB effectiveness of adsorption on OVS-DBC-PO and OVS-DBC-BT POIPs. At the initial stage, both OVS-DBC-PO and OVS-DBC-BT POIPs rapidly absorb dyes. Subsequently, the adsorption efficiency continues to increase, and after 48 h of adsorption, the curve reaches a plateau. This suggests that both adsorbents possess abundant adsorption sites and can effectively adsorb dyes even after an extended period.

3.3. The adsorption isotherm on the removal of RhB using OVS-DBC-PO and OVS-DBC-BT POIPs

Studying adsorption isotherm models is crucial for knowing the adsorption procedure and evaluating the efficiency of the used adsorbent. In batch mode studies, a sequence of RhB different concentrations of dye solutions ranging from 10 to 150 mg/L were prepared. Equal amounts of two POIPs were added to each dye solution and stirred at a steady temperature until the point of equilibrium was attained. Then, using a UV-visible spectrophotometer, the RhB equilibrium concentration in the solution was determined. The connection between the q_e (adsorption capacity) and C_e (equilibrium adsorbate concentration) of OVS-DBC-BT and OVS-DBC-PO POIPs for the adsorption of RhB is

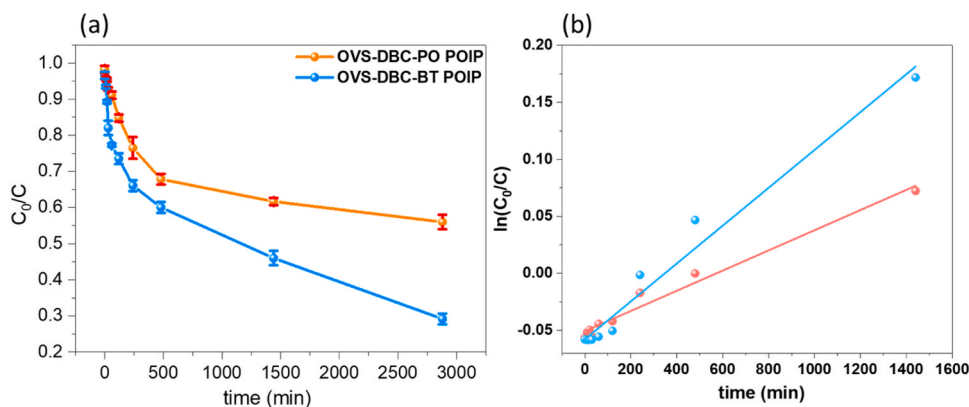


Fig. 8. (a) RhB's adsorption process using OVS-DBC-PO and OVS-DBC-BT POIP, and (b) kinetic information for that procedure. Dye concentration = 25 ppm; adsorbent mass = 0.5 g/L; pH=4.

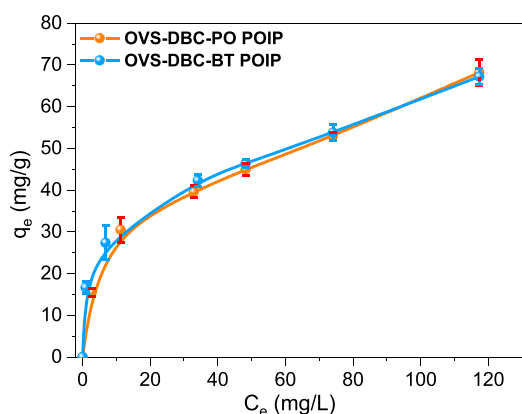


Fig. 9. Adsorption isotherm of RhB dye onto OVS-DBC-PO and OVS-DBC-BT POIPs. adsorbent mass = 0.5 g/L; pH=4; contact time= 24 h.

presented in Fig. 9. It was observed that increasing the concentration of RhB resulted in higher adsorption capacities of the OVS-POIPs, reaching stability at higher C_e values. As the RhB concentration increased, the mass driving force also increased, leading to a higher adsorption capacity of the POIPs. Consequently, with increased adsorption capacity, more adsorbate molecules could be absorbed on the surface of the OVS-POIPs. These findings demonstrate the potential of OVS-POIPs in removing Rhodamine B from the solution.

The isotherm model is the most complete and direct equation utilized to explain the adsorption process. In Fig. 10(a-d), the RhB adsorption data by POIPs is analyzed using the Langmuir and Freundlich isotherm models. Eq. (1) is the linearity of the Langmuir model:

$$\frac{C_e}{q_e} = \frac{1}{q_{\max} \times K_L} + \frac{C_e}{q_{\max}} \quad (1)$$

The maximum adsorption capacity of OVS-POIPs is denoted by q_{\max} , which is also quantified in mg/g. The adsorption energy and capacity are correlated with the Langmuir isotherm constants, expressed as K_L (L/mg). Eq. (2) is the linear equation of the Freundlich model. The adsorption energy and capacity are related to the Freundlich (K_F , $\text{mg}^{1-n} \text{L}^n/\text{g}$). The relevant calculated values are recorded in Table 1.

$$\log q_e = \log K_F + \frac{1}{n} \log C_e \quad (2)$$

According to the Freundlich isotherm model, both correlation coefficients (R^2) of OVS-DBC-PO and OVS-DBC-BT POIPs are 0.97 and 0.98 which is significantly larger than the Langmuir isotherm (R^2 is 0.90, and 0.94 respectively). This demonstrates that rhodamine B's adsorption by

the two POIPs occurs in multiple layers [78].

Non-linear fittings of the adsorption isotherm data of RhB onto OVS-DBC-PO and OVS-DBC-BT POIPs to the examined adsorption isotherm models are depicted in Figure S11. The resulting R^2 values, isotherm parameters (K_F , n , K_L , q_m , A_T , B , K_R , b_R , and g), chi-square (χ^2), and standard errors are presented in Table S4. It is evident that the Redlich-Peterson model not only achieved the highest correlation coefficient values ($R^2 = 0.949$ for OVS-DBC-PO POIP and 0.995 for OVS-DBC-BT POIP), but also the lowest χ^2 and standard error values. Therefore, the adsorption isotherms of RhB are best described by the Redlich-Peterson equation. This hybrid isotherm model effectively represents adsorption equilibria across a broad range of concentrations and applies to both homogeneous and heterogeneous systems. The g values from the Redlich-Peterson model in this study (Table S4) fall between 0 and 1 ($g = 0.918$ for OVS-DBC-PO POIP and 0.724 for OVS-DBC-BT POIP), indicating favorable adsorption of RhB onto the OVS-POIP materials.

3.4. The kinetic studies on the removal of RhB dye using OVS-DBC-PO and OVS-DBC-BT POIPs

To investigate the mechanisms of substance removal from aqueous solutions, particularly dye adsorption, different models of mathematics are commonly utilized for kinetic data analysis [79,80]. Among these models, the Lagergren rate equation (Eq. 3) is widely utilized. Here is the representation of the Lagergren rate equation:

$$\frac{dq_t}{dt} = k_1(q_e - q_t) \quad (3)$$

Eq. (1) shows that the dye concentration (mg/g) during the adsorption process at equilibrium and at a certain moment is denoted by the variables q_e and q_t , respectively. The dye's pseudo-first-order adsorption equilibrium rate constant is represented by the value k_1 . To obtain Eq. 4, restrict the integration of Eq. 3 to the intervals $t = 0$ to t and $q = 0$ to q_t .

$$\ln(q_e - q_t) = \ln q_e - k_1 t \quad (4)$$

To find k_1 for RhB adsorption capacity on the two OVS-POIP adsorbents, $\ln(q_e - q_t)$ is plotted against time (t) in Figs. 11(a) and 11(b). Table 2 displays the computed values. Ho and McKay's suggested equation is used to determine the pseudo-second-order dynamics. The following is the expression for the differential Eq. 4:

$$\frac{dq_t}{dt} = k_2(q_e - q_t)^2 \quad (4)$$

The pseudo-secondary adsorption equilibrium's rate constant is k_2 ($\text{g}/(\text{mg} \cdot \text{min})$). When Eq. (4) is integrated from $t = 0$ to $t = q_t$, Eq. 5 is obtained.

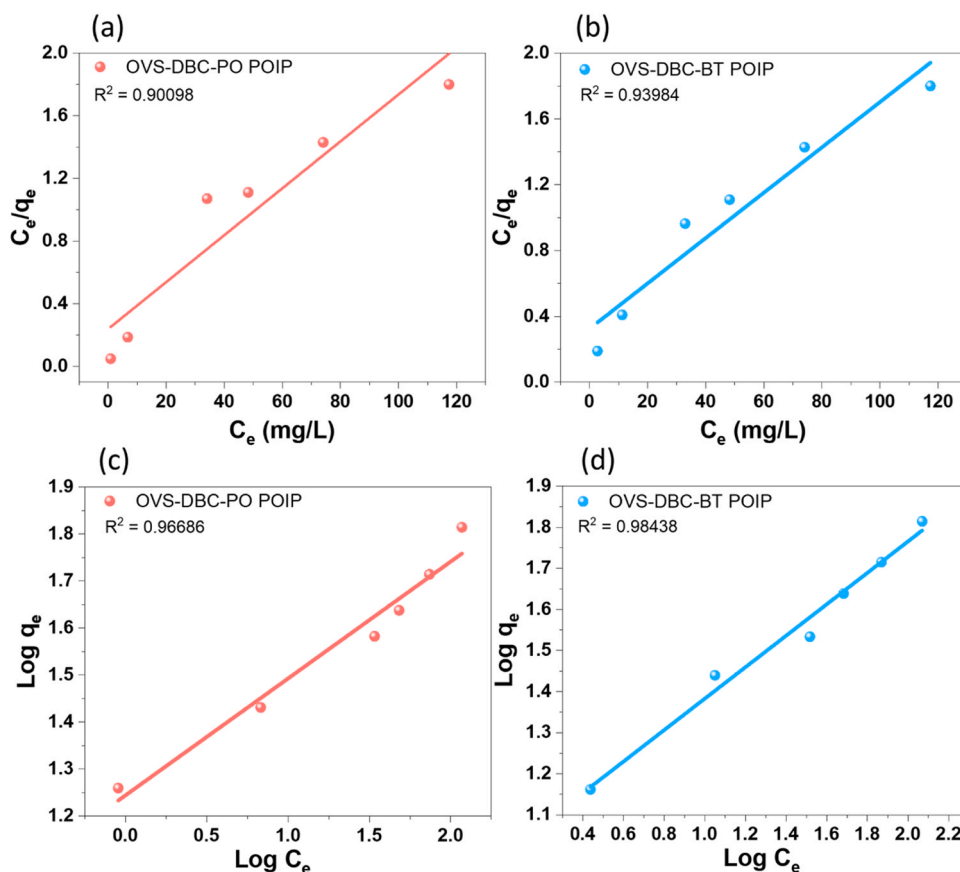


Fig. 10. (a-b) Langmuir and (c-d) Freundlich fitting of (a, c) OVS-DBC-PO and (b, d) OVS-DBC-BT POIPs.

Table 1

Rhodamine B adsorption isotherm parameters on OVS-DBC-PO and OVS-DBC-BT POIPs.

Adsorbent	Langmuir			Freundlich		
	q_{max} (mg g^{-1})	K_L (L/mg)	R^2	K_F (mg $^{1-n}$ L n /g)	1/n	R^2
OVS-DBC-PO POIP	66.80	0.0626	0.90	17.548	0.24861	0.97
OVS-DBC-BT POIP	72.57	0.042	0.94	9.999	0.38274	0.98

$$\frac{1}{q_e - q_t} = \frac{1}{q_e} + k_2 t \quad (5)$$

Eq. 6 illustrates a pseudo-second-order reaction's integral rate law. A linear form can be obtained by rearranging it [70]:

$$\frac{t}{q_t} = \frac{1}{k_2 q_e^2} + \left(\frac{1}{q_e}\right)t \quad (6)$$

Figs. 11(c) and 11(d) depict linear graphs of time versus t/q_t . These graphs facilitate the calculation of k_2 , q_e , and correlation coefficient values for the solution of dye, which are listed in Table 2. It is demonstrated that pseudo-first-order kinetics describe the adsorption of RhB by OVS-DBC-PO and OVS-DBC-BT POIPs more correctly than pseudo-second-order kinetics. This observation implies that physical adsorption mechanisms primarily control the adsorption process. The non-linear fittings of the kinetic data for the studied RhB to the three kinetic models (pseudo-first-order, pseudo-second-order, and Elovich) are illustrated in Figure S12. The calculated kinetic parameter values are listed in Table S5. This table shows that the kinetic models fit the kinetic data of RhB well with the two polymers, achieving high correlation

coefficient values ($R^2 \approx 0.97$ and 0.99) for OVS-DBC-PO and OVS-DBC-BT POIPs, respectively. To identify the most suitable kinetic model for the current data, standard error values were considered. By comparing these error function values, it is evident that the Elovich model is the best fit for describing the kinetic data of RhB with OVS-DBC-PO POIP and OVS-DBC-BT POIP. The recyclability assessments for the samples OVS-DBC-PO POIP and OVS-DBC-BT POIP, which are highlighted as the most promising, indicate that these samples maintained high RhB removal efficiencies of up to 96 % even after six experimental cycles, as depicted in Figure S13. To evaluate the stability of both POIPs over six cycles, as illustrated in Figures S14 and S15, the absorption bands associated with aromatic CH, C=C, and O-Si-O remain present in the frameworks of OVS-DBC-PO POIP and OVS-DBC-BT POIP. Table S6 displays a contrast between the dye adsorption capacities of OVS-DBC-PO and OVS-DBC-BT POIPs and those of other materials. When the system was exposed to varying temperatures, a notable trend emerged: the adsorption of Rhodamine B onto OVS-DBC-PO and OVS-DBC-BT POIPs significantly increased as the temperature rose from 30 to 70 °C [Figs. 12(a) and 12(b)]. This finding highlights the temperature-dependent nature of the adsorption process, indicating that temperature directly influences the adsorption behavior of Rhodamine B on OVS-DBC-PO and OVS-DBC-BT POIPs.

To gain a deeper understanding of the thermodynamics of this adsorption process, various thermodynamic parameters were calculated using Eqs. (7–9). These crucial parameters include the enthalpy change (ΔH°), entropy change (ΔS°), and free energy (ΔG°). These thermodynamic analyses offer essential insights into the energetics and spontaneity of the adsorption of Rhodamine B onto OVS-DBC-PO and OVS-DBC-BT POIPs, providing a clearer understanding of the mechanisms underlying this interaction.

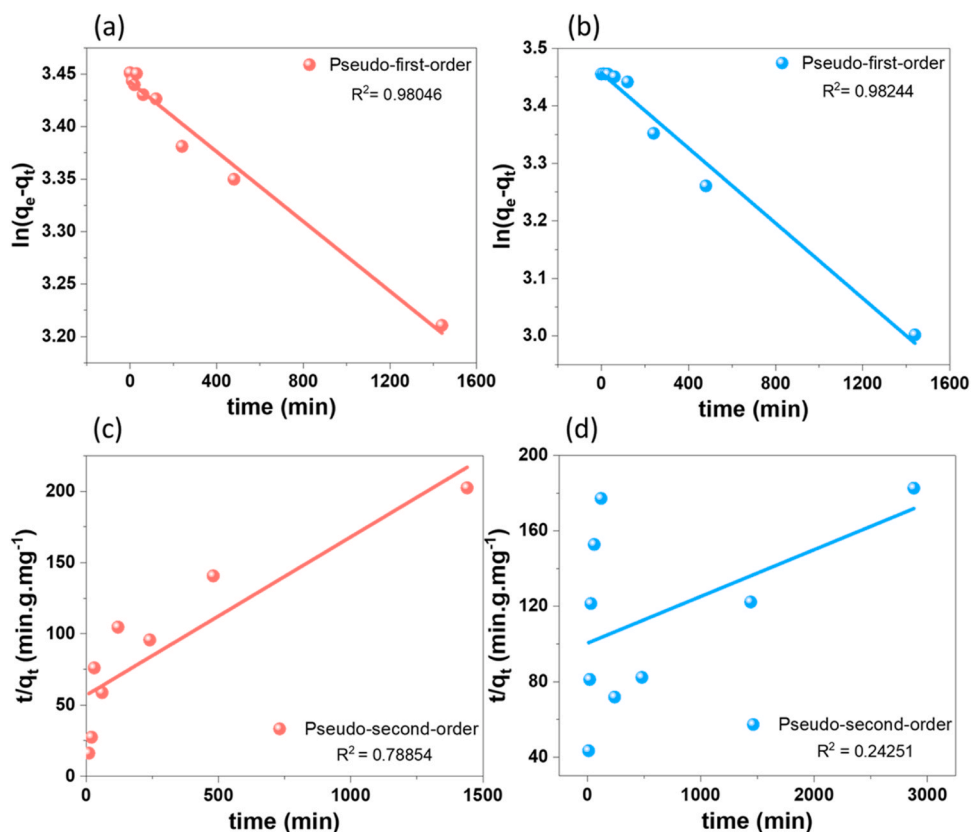


Fig. 11. . (a-b) Pseudo-first-order kinetic and (c-d) Pseudo-second-order kinetic fitting of (a, c) OVS-DBC-PO and (b, d) OVS-DBC-BT POIPs.

Table 2

Rhodamine B adsorption kinetic parameters on OVS-DBC-PO and OVS-DBC-BT POIPs.

Adsorbent	Pseudo-first-order			Pseudo-second-order		
	qe1 (mg g ⁻¹)	k1 (min ⁻¹)	R ²	qe2 (mg g ⁻¹)	k2 (g mg ⁻¹ min ⁻¹)	R ²
OVS-DBC-PO POIP	31.26	0.000166	0.98	9.01	0.000216	0.78
OVS-DBC-BT POIP	31.71	0.000359	0.98	40.37	0.0000061	0.24

$$\ln K_d = \frac{\Delta S^\circ}{R} - \frac{\Delta H^\circ}{RT} \quad (7)$$

$$K_d = \left(\frac{C_i - C_f}{A_f} \right) \times \frac{V}{M} \quad (8)$$

Table 3

Thermodynamic parameters for adsorption of Rhodamine B onto OVS-DBC-PO and OVS-DBC-BT POIPs.

Polymer	ΔG° (kJ mol ⁻¹)			ΔH° (kJ mol ⁻¹)	ΔS° (kJ mol ⁻¹ K ⁻¹)	R ²
	303 K	323 K	333 K			
OVS-DCB-PO POIP	-22.512	-24.314	-25.357	5.986	0.094	0.968
OVS-DCB-BT POIP	-22.479	-24.039	-24.809	1.069	0.078	0.996

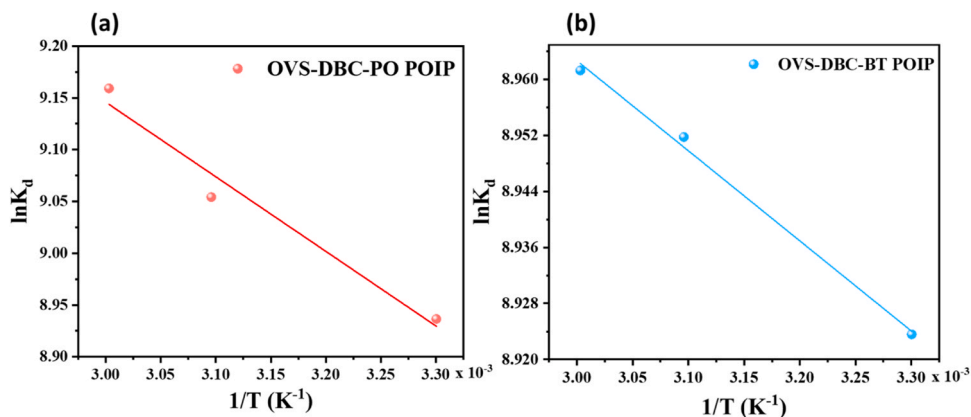


Fig. 12. Plot of $\ln K_d$ versus $1/T$ for adsorption of Rhodamine B onto (a) OVS-DBC-PO and (b) OVS-DBC-BT POIPs.

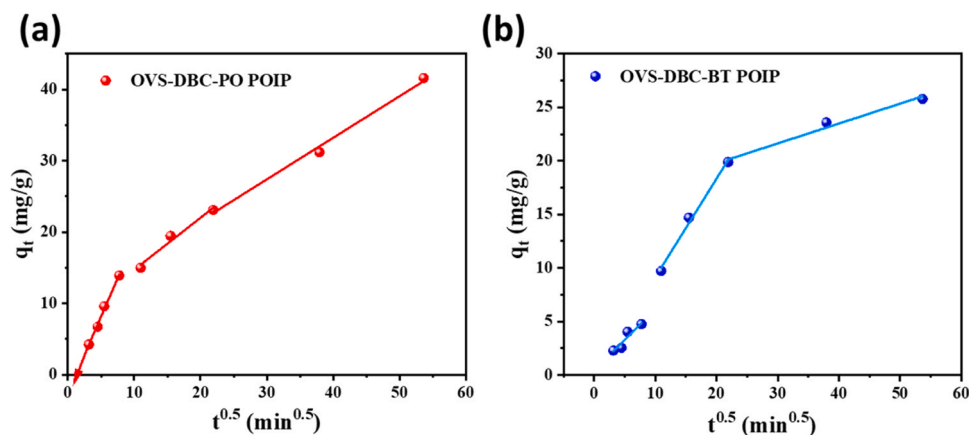


Fig. 13. Intraparticle diffusion of RhB dye onto (a) OVS-DBC-PO and (b) OVS-DBC-BT POIP.

$$\Delta G^\circ = -RT \ln K_d \quad (9)$$

The linear plot of $\ln K_d$ against $1/T$, shown in Fig. 12, was instrumental in determining the thermodynamic parameters of interest. The slope and intercept of this plot were used to calculate the enthalpy change (ΔH°) and entropy change (ΔS°), respectively. Table 3 summarizes the computed thermodynamic values for the adsorption of Rhodamine B onto OVS-DBC-PO and OVS-DBC-BT POIPs. The negative values of ΔG° at various temperatures indicate that the adsorption process is both feasible and spontaneous. The positive ΔH° value suggests that the adsorption is endothermic. Additionally, the positive ΔS° value implies an increase in randomness or entropy during the adsorption of Rhodamine B onto OVS-POIPs [81,82]. This indicates that the system becomes more disordered as adsorption occurs, providing insights into the thermodynamic nature of the process.

The mechanism of adsorption was examined to understand the nature of the adsorption process. This was accomplished through the intraparticle diffusion model. The rate of adsorption is influenced by three controlling factors: (i) mass transfer across the external boundary (the dye molecule moved to the outer surface of adsorbent polymer), (ii) adsorption at the internal and external surfaces (the dye gets into the pores of adsorbent polymer) which depends on the binding process, and (iii) movement of the adsorbate to the adsorption site (the adsorption takes place on the surface on the polymer). A linear relationship was observed in the plot of q_t against $t^{0.5}$ for the uptake of RhB, although it did not intersect the origin, as shown in Fig. 13. This suggests that boundary layer diffusion contributes to the adsorption of RhB onto the polymer, indicating that intraparticle diffusion is not the sole rate-controlling step in the adsorption process.

The constituents of the OVS-DBC-PO and OVS-DBC-BT POIP contain various active functional groups that significantly affect the adsorption or removal of dyes. This process involves interaction or binding between the solid surface of the adsorbent and the adsorbate. There are two primary factors affecting the adsorption process: the structure of the adsorbate and the functional groups present on the adsorbent surface. RhB, a cationic dye, contains two amino groups and one carboxylic group. These functional groups could facilitate the uptake of positively charged RhB molecules. The π electrons in the POIPs and the cationic dyes participate in electrostatic interactions. The planar structure of the RhB molecule facilitates its adsorption due to π - π interactions between the aromatic backbones of the dyes and the POIP materials, as illustrated in Figures S16 and S17.

4. Conclusions

In summary, the Heck reaction was employed to synthesize two distinct types of OVS POIPs: OVS-DBC-PO and OVS-DBC-BT POIPs. Upon comparison, OVS-DBC-BT POIP outperforms OVS-DBC-PO POIP in terms

of S_{BET} ($386 \text{ m}^2 \text{ g}^{-1}$) and T_{d10} is $543 \text{ }^\circ\text{C}$. Following an adsorption experiment, it was noted that the amount of RhB present in the watery solution was lower for OVS-DBC-BT POIP compared to OVS-DBC-PO POIP, indicating a higher adsorption capacity for the former. Under optimal conditions, the maximal adsorption capacities of the OVS-DBC-PO, and OVS-DBC-BT POIPs precursors were confirmed to be 65 and 66 mg/g, respectively. This was achieved by employing 0.5 g/L of OVS-POIP materials with RhB (25 ppm) at $25 \text{ }^\circ\text{C}$. In the kinetics and isothermal adsorption studies, both OVS-DBC-PO and OVS-DBC-BT POIPs exhibited a better fit with the pseudo-first-order kinetics and the Freundlich isotherm. These results suggest that physical multilayer adsorption mechanisms primarily dominate the adsorption processes. Motivated by the remarkable findings of this study, our group is inspired to explore efficient synthetic methods for the development of OVS-based POIP materials aimed at treating and purifying water. We are particularly interested in leveraging the favorable high porosity resulting from the distinctive molecular characteristics of these building monomers [OVS, DBC, PO, and BT].

CRedit authorship contribution statement

Ching Wen Hsiao: Formal analysis, Data curation, Conceptualization, Investigation, Supervision. **Shiao-wei Kuo:** Supervision. **Mohammed G. Kotp:** Formal analysis, Investigation. **Ahmed M. Elewa:** Formal analysis, Data curation. **Mohamed Gamal Mohamed:** Writing – review & editing, Writing – original draft, Supervision, Methodology, Investigation, Formal analysis, Data curation, Conceptualization. **Mitch Ming-Chi Chou:** Conceptualization.

Declaration of Competing Interest

The authors declare that they have no known competing financial interests or personal relationships that could have appeared to influence the work reported in this paper.

Data availability

The data that has been used is confidential.

Acknowledgements

This study was supported financially by the National Science and Technology Council, Taiwan, under contracts NSTC 112-2223-E-110-002- and 112-2218-E-110-007. The authors thank the staff at National Sun Yat-sen University for their assistance with the TEM (ID: EM022600) experiments.

Appendix A. Supporting information

Supplementary data associated with this article can be found in the online version at [doi:10.1016/j.colsurfa.2024.134658](https://doi.org/10.1016/j.colsurfa.2024.134658).

References

- W.A. Al-Amrani, S.A. Onaizi, Adsorptive removal of heavy metals from wastewater using emerging nanostructured materials: a state-of-the-art review, *Sep. Purif. Technol.* 343 (2024) 127018, <https://doi.org/10.1016/j.seppur.2024.127018>.
- M. Afshari, M. Dinari, Synthesis of new imine-linked covalent organic framework as high efficient adsorbent and monitoring the removal of direct fast scarlet 4BS textile dye based on mobile phone colorimetric platform, *J. Hazard. Mater.* 385 (2020) 121514, <https://doi.org/10.1016/j.jhazmat.2019.121514>.
- F.S.A. Khan, N.M. Mubarak, Y.H. Tan, M. Khalid, R.R. Karri, R. Walvekar, E. C. Abdullah, S. Nizamuddin, S.A. Mazari, A comprehensive review on magnetic carbon nanotubes and carbon nanotube-based buckypaper for removal of heavy metals and dyes, *J. Hazard. Mater.* 413 (2021) 125375, <https://doi.org/10.1016/j.jhazmat.2021.125375>.
- H. Xue, X.S. Huang, Q. Yin, X.J. Hu, H.Q. Zheng, G. Huang, T.F. Liu, Bimetallic cationic metal-organic frameworks for selective dye adsorption and effective $\text{Cr}_2\text{O}_7^{2-}$ removal, *Cryst. Growth Des.* 20 (2020) 4861–4866, <https://doi.org/10.1021/acs.cgd.0c00239>.
- K.K. Thasneema, T. Dipin, M.S. Thayyil, P.K. Sahu, M. Messali, T. Rosalin, K. K. Elyas, P.M. Saharuba, T. Anjitha, T.B. Hadda, Removal of toxic heavy metals, phenolic compounds and textile dyes from industrial waste water using phosphonium based ionic liquids, *J. Mol. Liq.* 323 (2021) 114645, <https://doi.org/10.1016/j.molliq.2020.114645>.
- D. Lan, H. Zhu, J. Zhang, S. Li, Q. Chen, C. Wang, T. Wu, M. Xu, Adsorptive removal of organic dyes via porous materials for wastewater treatment in recent decades: a review on species, mechanisms and perspectives, *Chemosphere* 293 (2022) 133464, <https://doi.org/10.1016/j.chemosphere.2021.133464>.
- Z. Ma, H. Chang, Y. Liang, Y. Meng, L. Ren, H. Liang, Research progress and trends on state-of-the-art membrane technologies in textile wastewater treatment, *Sep. Purif. Technol.* 333 (2024) 125853, <https://doi.org/10.1016/j.seppur.2023.125853>.
- W. Wang, Y. Lv, H. Liu, Z. Cao, Recent advances in application of polypyrrole nanomaterial in water pollution control, *Sep. Purif. Technol.* 330 (2024) 125265, <https://doi.org/10.1016/j.seppur.2023.125265>.
- C. Wei, Y. Cai, Z. Yang, A bifunctional imidazolium-based porous organic polymer for efficient detection of $\text{Cr}_2\text{O}_7^{2-}$ and adsorptive separation of $\text{Cr}_2\text{O}_7^{2-}$ and MO in water, *J. Water Process Eng.* 57 (2024) 104573 <https://doi.org/10.1016/j.jwpe.2023.104573>.
- M. Ge, H. Liu, Fluorine-Containing Silsesquioxane-Based Hybrid Porous Polymers Mediated by Bases and Their Use in Water Remediation, *Chem. Eur. J.* 24 (2018) 2224–2231, <https://doi.org/10.1002/chem.201705192>.
- R. Das, C.D. Vecitis, A. Schulze, B. Cao, A.F. Ismail, X. Lu, J. Chen, S. Ramakrishna, Recent advances in nanomaterials for water protection and monitoring, *Chem. Soc. Rev.* 46 (2017) 6946–7020, <https://doi.org/10.1039/C6CS00921B>.
- Y. Liu, Y. Cui, C. Zhang, J. Du, S. Wang, Y. Bai, Z. Liang, X. Song, Post-cationic modification of a pyrimidine-based conjugated microporous polymer for enhancing the removal performance of anionic dyes in water, *Chem. Eur. J.* 24 (2018) 7480–7488, <https://doi.org/10.1002/chem.201800548>.
- A.A. Al-Gheethi, Q.M. Azhar, P. Senthil Kumar, A.A. Yusuf, A.K. Al-Buriah, R.M. S. Radin Mohamed, M.M. Al-Shaibani, Sustainable approaches for removing Rhodamine B dye using agricultural waste adsorbents: a review, *Chemosphere* 287 (2022) 132080, <https://doi.org/10.1016/j.chemosphere.2021.132080>.
- L. Jin, Y.L. Li, J. Zhou, C.M. Huang, X. Liu, Rhodamine B as an efficient multifunctional passivator for the improvement of perovskite solar cell performance, *J. Mater. Chem. C* 11 (2023) 9189–9200, <https://doi.org/10.1039/D3TC00818E>.
- L.M. Skjolding, K.S. Dyhr, C.J. Köppl, U.S. McKnight, P. Bauer-Gottwein, P. Mayer, A. Baun, Assessing the aquatic toxicity and environmental safety of tracer compounds Rhodamine B and Rhodamine WT, *Water Res.* 197 (2021) 117109, <https://doi.org/10.1016/j.watres.2021.117109>.
- Z. Chai, B. Liu, P. Lv, Y. Bai, J. Wang, X. Song, W. Su, G. Yu, Recycling of coal gasification fine slag as ultra-high capacity adsorbents for the removal of Rhodamine B dye: Graded synthesis method, kinetics and adsorption mechanism, *Fuel* 333 (2023) 126318, <https://doi.org/10.1016/j.fuel.2022.126318>.
- U. Jinendra, D. Bilehal, B.M. Nagabhushana, A.P. Kumar, Adsorptive removal of Rhodamine B dye from aqueous solution by using graphene-based nickel nanocomposite, *Heliyon* 7 (2021) e06851 <https://doi.org/10.1016/j.heliyon.2021.e06851>.
- R.D. Saini, Textile organic dyes: polluting effects and elimination methods from textile wastewater, *Int. J. Chem. Eng. Res.* 9 (2017) 121–136, <https://doi.org/10.5772/32373>.
- S.S. Vedula, G.D. Yadav, Treatment of wastewater containing alizarin red dye: development and application of magnetic chitosan as a natural eco-friendly material, *Clean. Techn. Environ. Policy* 25 (2023) 865–878, <https://doi.org/10.1007/s10098-022-02408-9>.
- W.S. Koe, J.W. Lee, W.C. Chong, Y.L. Pang, L.C. Sim, An overview of photocatalytic degradation: photocatalysts, mechanisms, and development of photocatalytic membrane, *Environ. Sci. Pollut. Res.* 27 (2020) 2522–2565, <https://doi.org/10.1007/s11356-019-07193-5>.
- T.O. Ajiboye, O.A. Oyewo, D.C. Onwudiwe, Adsorption and photocatalytic removal of Rhodamine B from wastewater using carbon-based materials, *FlatChem* 29 (2021) 100277, <https://doi.org/10.1016/j.flatc.2021.100277>.
- L. Peng, P. Qin, M. Lei, Q. Zeng, H. Song, J. Yang, J. Shao, B. Liao, J. Gu, Modifying Fe_3O_4 nanoparticles with humic acid for removal of Rhodamine B in water, *J. Hazard. Mater.* 209 (2012) 193–198, <https://doi.org/10.1016/j.jhazmat.2012.01.011>.
- X. Zhao, D. Wang, C. Xiang, F. Zhang, L. Liu, X. Zhou, H. Zhang, Facile synthesis of boron organic polymers for efficient removal and separation of methylene blue, rhodamine B, and rhodamine 6G, *ACS Sustain. Chem. Eng.* 6 (2018) 16777–16787, <https://doi.org/10.1021/acssuschemeng.8b04049>.
- X.-C. Du, J.-H. Zhu, Z.-J. Quan, X.-C. Wang, Adsorption of rhodamine B by organic porous materials rich in nitrogen, oxygen, and sulfur heteroatoms, *N. J. Chem.* 45 (2021) 3448–3453, <https://doi.org/10.1039/D0NJ05750A>.
- Y. Han, W. Li, J. Zhang, H. Meng, Y. Xu, X. Zhang, Adsorption behavior of Rhodamine B on nanoporous polymers, *RSC Adv.* 5 (2015) 104915–104922, <https://doi.org/10.1039/C5RA21130A>.
- H. Wang, N. Qiu, X. Kong, Z. Hu, F. Zhong, Y. Li, H. Tan, Novel Carbazole-Based Porous Organic Polymer for Efficient Iodine Capture and Rhodamine B Adsorption, *ACS Appl. Mater. Interfaces* 15 (2023) 14846–14853, <https://doi.org/10.1021/acsaami.3c00918>.
- E. Forgacs, T. Cserhádi, G. Oros, Removal of synthetic dyes from wastewaters: a review, *Environ. Int.* 30 (2004) 953–971, <https://doi.org/10.1016/j.envint.2004.02.001>.
- M.G. Mohamed, A.F.M. EL-Mahdy, T.S. Meng, M.M. Samy, S.W. Kuo, Multifunctional Hypercrosslinked Porous Organic Polymers Based on Tetraphenylethene and Triphenylamine Derivatives for High-Performance Dye Adsorption and Supercapacitor, *Polymers* 12 (2020) 2426, <https://doi.org/10.3390/polym12102426>.
- M. Zhang, Y. Du, H. Liu, Porous hybrid triazine-functionalized polymers with high capture ability for I_2 and dyes, *ACS Appl. Polym. Mater.* 5 (2023) 654–661, <https://doi.org/10.1021/acsapm.2c01709>.
- P.P. Selvam, S. Preethi, P. Basakaringam, N. Thinakaran, A. Sivasamy, S. Sivanesan, Removal of rhodamine B from aqueous solution by adsorption onto sodium montmorillonite, *J. Hazard. Mater.* 155 (2008) 39–44, <https://doi.org/10.1016/j.jhazmat.2007.11.025>.
- Y. Zhao, L. Zhu, W. Li, J. Liu, X. Liu, K. Huang, Insights into enhanced adsorptive removal of Rhodamine B by different chemically modified garlic peels: comparison, kinetics, isotherms, thermodynamics and mechanism, *J. Mol. Liq.* 293 (2019) 111516, <https://doi.org/10.1016/j.molliq.2019.111516>.
- A.M. Elgarahy, M.G. Eloffy, E. Guibal, H.M. Alghamdi, K.Z. Elwakeel, Use of biopolymers in wastewater treatment: a brief review of current trends and prospects, *Chin. J. Chem. Eng.* 64 (2023) 292–320, <https://doi.org/10.1016/j.cjche.2023.05.018>.
- Z.A. Khan, K.Z. Elwakeel, R.A. Mashabi, A.M. Elgarahy, Adsorption of anionic dyes onto 1,5-Diphenylcarbazide functionalized magnetic hybrid polymer: impact of water salinity and surfactants on adsorption isotherms, *J. Ind. Eng. Chem.* 131 (2024) 569–584, <https://doi.org/10.1016/j.jiec.2023.10.061>.
- Buhani, J.S. Dewi, N.S. Fajriyah, M. Rilyanti, Suharso, Sumadi, K.Z. Elwakeel, Modification of Non-Activated Carbon from Rubber Fruit Shells with 3-(Aminopropyl)-Triethoxysilane and Its Adsorption Study on Coomassie Brilliant Blue and Methylene Blue in Solution, *Water Air Soil Pollut.* 234 (2023) 578, <https://doi.org/10.1007/s11270-023-06506-2>.
- A.M. Elgarahy, H.Y. Mostafa, E.G. Zaki, S.M. ElSaeed, K.Z. Elwakeel, A. Akhdhar, E. Guibal, Methylene blue removal from aqueous solutions using a biochar/gellan gum hydrogel composite: Effect of agitation mode on sorption kinetics, *Int. J. Biol. Macromol.* 232 (2023) 123355, <https://doi.org/10.1016/j.ijbiomac.2023.123355>.
- R.A. Mashabi, Z.A. Khan, K.Z. Elwakeel, Chitosan- or glycidyl methacrylate-based adsorbents for the removal of dyes from aqueous solutions: a review, *Mater. Adv.* 3 (2022) 5645–5671, <https://doi.org/10.1039/D2MA00320A>.
- Y. Du, H. Liu, Cage-like Silsesquioxanes-Based Hybrid Materials, *Dalton Trans.* 49 (2020) 5396–5405, <https://doi.org/10.1039/D0TD00587H>.
- M.G. Mohamed, S.W. Kuo, Progress in the self-assembly of organic/inorganic polyhedral oligomeric silsesquioxane (POSS) hybrids, *Soft Matter* 18 (2022) 5535–5561, <https://doi.org/10.1039/D2SM00635A>.
- X. Lin, Y.Y. Deng, Q. Zhang, D. Han, Q. Fu, Effect of POSS Size on the Porosity and Adsorption Performance of Hybrid Porous Polymers, *Macromolecules* 56 (2023) 1243, <https://doi.org/10.1021/acs.macromol.2c02486>.
- C.Y. Chen, W.C. Chen, M.G. Mohamed, Z.Y. Chen, S.W. Kuo, Highly thermally stable, reversible and flexible main chain-type benzoxazine hybrid incorporating both polydimethylsiloxane and double-decker-shaped polyhedral silsesquioxane, *Macromol. Rapid Commun.* 44 (2023) 2200910, <https://doi.org/10.1002/marc.202200910>.
- S. Takase, T. Hamada, K. Okada, S. Mineoi, J. Ohshita, Polysilsesquioxane-containing thermally degradable groups for potential application as thermal insulation materials, *ACS Appl. Polym. Mater.* 5 (2023) 1390, <https://doi.org/10.1021/acsaapm.2c01900>.
- C.H. Chiang, M.G. Mohamed, W.C. Chen, M. Madhu, W.L. Tseng, S.W. Kuo, Construction of fluorescent conjugated polytriazole containing double-decker silsesquioxane: click polymerization and thermal stability, *Polymers* 15 (2023) 331, <https://doi.org/10.3390/polym15020331>.
- M.G. Mohamed, S.W. Kuo, Functional silica and carbon nanocomposites based on polybenzoxazines, *Macromol. Chem. Phys.* 220 (2019) 1800306, <https://doi.org/10.1002/macp.201800306>.

- [44] M.G. Mohamed, S.W. Kuo, Functional polyimide/polyhedral oligomeric silsesquioxane nanocomposites, *Polymers* 11 (2019) 26, <https://doi.org/10.3390/polym11010026>.
- [45] X. Lin, W.H. Siew, J. Ligat, M. Given, J. He, J. Octavinyl polyhedral oligomeric silsesquioxane on tailoring the DC electrical characteristics of polypropylene, *High. Volt.* 7 (2021) 137–146, <https://doi.org/10.1049/hve2.12146>.
- [46] A. Kausar, State-of-the-art overview on polymer/POSS nanocomposite, *Polym. Plast. Technol. Eng.* 56 (2017) 1401–1420, <https://doi.org/10.1080/03602559.2016.1276592>.
- [47] N. Ahmed, H. Fan, P. Dubois, X. Zhang, S. Fahad, T. Aziz, J. Wan, Nano-engineering and micromolecular science of polysilsesquioxane materials and their emerging applications, *J. Mater. Chem. A* 7 (2019) 21577–21604, <https://doi.org/10.1039/C9TA04575A>.
- [48] M. Ejaz, M.M. Samy, Y. Ye, S.W. Kuo, M.G. Mohamed, Design hybrid porous organic/inorganic polymers containing polyhedral oligomeric silsesquioxane/pyrene/anthracene moieties as a high-performance electrode for supercapacitor, *Int. J. Mol. Sci.* 24 (2023) 2501, <https://doi.org/10.3390/ijms24032501>.
- [49] M.G. Mohamed, M.H. Elsayed, Y. Ye, M.M. Samy, A.E. Hassan, T.H. Mansoure, Z. Wen, H.H. Chou, K.H. Chen, S.W. Kuo, Construction of porous organic/inorganic hybrid polymers based on polyhedral oligomeric silsesquioxane for energy storage and hydrogen production from water, *Polymers* 15 (2023) 182, <https://doi.org/10.3390/polym15010182>.
- [50] P. Loganathan, K.K.R. Datta, S. Shanmugan, A superhydrophobic covalent zeolitic imidazolate framework-polyhedral oligomeric silsesquioxane hybrid material as a highly efficient and reusable sorbent for organic solvents, *Inorg. Chem. Front.* 8 (2021) 2288–2298, <https://doi.org/10.1039/D0QI01405B>.
- [51] D.B. Cordes, P.D. Lickiss, F. Rataboul, Recent developments in the chemistry of cubic polyhedral oligosilsesquioxanes, *Chem. Rev.* 110 (2010) 2081–2173, <https://doi.org/10.1021/cr900201r>.
- [52] M.G. Mohamed, M.Y. Tsai, C.F. Wang, C.F. Huang, M. Danko, L. Dai, T. Chen, S. W. Kuo, Multifunctional polyhedral oligomeric silsesquioxane (POSS) based hybrid porous materials for CO₂ uptake and iodine adsorption, *Polymers* 13 (2021) 221, <https://doi.org/10.3390/polym13020221>.
- [53] D. Yang, W. Zhang, R. Yao, B. Jiang, Thermal stability enhancement mechanism of poly(dimethylsiloxane) composite by incorporating octavinyl polyhedral oligomeric silsesquioxanes, *Polym. Degrad. Stab.* 98 (2013) 109–114, <https://doi.org/10.1016/j.polydegradstab.2012.10.021>.
- [54] T. Nakano, H. Imoto, K. Naka, AB-type monomer of polyhedral oligomeric silsesquioxane, *Inorg. Chem. Front.* 11 (2024) 1781–1788, <https://doi.org/10.1039/D3QI02674D>.
- [55] M. Soldatov, H. Liu, Hybrid porous polymers based on cage-like organosiloxanes: synthesis, properties and applications, *Prog. Polym. Sci.* 119 (2021) 101419, <https://doi.org/10.1016/j.progpolymsci.2021.101419>.
- [56] Q. Ge, H. Liu, Open/Closed cage silsesquioxane-based thioamide-bridged hybrid networks with unexpected adsorption abilities and selectivity for Au (III), *Chem. Eng. J.* 462 (2023) 142323, <https://doi.org/10.1016/j.cej.2023.142323>.
- [57] M.G. Mohamed, M.M.M. Ahmed, W.-T. Du, S.-W. Kuo, Meso/microporous carbons from conjugated hyper-crosslinked polymers based on tetraphenylethene for high performance for CO₂ capture and supercapacitor, *Molecules* 26 (2021) 738, <https://doi.org/10.3390/molecules26030738>.
- [58] T.H. Weng, M.G. Mohamed, S.U. Sharma, S.V. Chaganti, M.M. Samy, J.T. Lee, S. W. Kuo, Ultrastable three-dimensional triptycene- and tetraphenylethene-conjugated microporous polymers for energy storage, *ACS Appl. Energy Mater.* 5 (2022) 14239–14249, <https://doi.org/10.1021/acsaem.2c02809>.
- [59] M.G. Mohamed, H.Y. Hu, S. Santhoshkumar, M. Madhu, T.H. Mansoure, C. W. Hsiao, Y. Ye, C.W. Huang, W.L. Tseng, S.W. Kuo, Design and synthesis of bifunctional conjugated microporous polymers containing tetraphenylethene and bisulfone units for energy storage and fluorescent sensing of p-nitrophenol, *Colloids Surf. A Physicochem. Eng. Asp.* 680 (2024) 132675, <https://doi.org/10.1016/j.colsurfa.2023.132675>.
- [60] M.M. Samy, M.G. Mohamed, S.U. Sharma, S.V. Chaganti, J.T. Lee, S.W. Kuo, An Ultrastable Tetrabenzenophthalene-Linked conjugated microporous polymer functioning as a high-performance electrode for supercapacitors, *J. Taiwan Inst. Chem. Eng.* (2024) 104750, <https://doi.org/10.1016/j.jtice.2023.104750>.
- [61] A.O. Mousa, Z.I. Lin, S.V. Chaganti, C.H. Chuang, C.K. Chen, S.W. Kuo, M. G. Mohamed, Bifunctional imidazolium linked tetraphenylethene based conjugated microporous polymers for dynamic antibacterial properties and supercapacitor electrodes, *Polym. Chem.* 15 (2024) 397–411, <https://doi.org/10.1039/D3PY01303K>.
- [62] M.G. Mohamed, M.H. Elsayed, C.J. Li, A.E. Hassan, I.M.A. Mekhemer, A.F. Musa, M.K. Hussien, L.C. Chen, K.H. Chen, H.H. Chou, S.W. Kuo, Reticular design and alkynyl bridge engineering in donor- π -acceptor type conjugated microporous polymers for boosting photocatalytic hydrogen evolution, *J. Mater. Chem. A* 12 (2024) 7693–7710, <https://doi.org/10.1039/D3TA07309B>.
- [63] H. Liu, H. Liu, Selective dye adsorption and metal ion detection using multifunctional silsesquioxane-based tetraphenylethene-linked nanoporous polymers, *J. Mater. Chem. A* 5 (2017) 9156–9162, <https://doi.org/10.1039/C7TA01255A>.
- [64] M. Gea, H. Liu, A silsesquioxane-based thiophene-bridged hybrid nanoporous network as a highly efficient adsorbent for wastewater treatment, *J. Mater. Chem. A* 4 (2016) 16714–16722, <https://doi.org/10.1039/C6TA06656A>.
- [65] C.W. Hsiao, A.M. Elewa, M.G. Mohamed, S.W. Kuo, Highly stable hybrid porous polymers containing polyhedral oligomeric silsesquioxane (POSS)/Dibenzo [g, p] chrysene and Dibenzo [b, d] thiophene units for efficient Rhodamine B dye removal, *Sep. Purif. Technol.* 332 (2024) 125771, <https://doi.org/10.1016/j.seppur.2023.125771>.
- [66] S. Kumar, S.K. Varshney, Dibenzo[g,p]chrysene, a novel core for discotic liquid crystals, *Mol. Cryst. Liq. Cryst.* 378 (2002) 59–64, <https://doi.org/10.1080/713738586>.
- [67] X.Y. Liu, X. Tang, Y. Zhao, D. Zhao, J. Fan, L.S. Liao, Dibenzo [g, p] chrysene: a new platform for highly efficient red phosphorescent organic light-emitting diodes, *Dyes Pigm.* 146 (2017) 234–239, <https://doi.org/10.1016/j.dyepig.2017.06.036>.
- [68] M.M. Samy, M.G. Mohamed, A.F.M. El-Mahdy, T.H. Mansoure, K.C.W. Wu, S. W. Kuo, High-performance supercapacitor electrodes prepared from dispersions of tetrabenzenophthalene-based conjugated microporous polymers and carbon nanotubes, *ACS Appl. Mater. Interfaces* 13 (2021) 51906–51916, <https://doi.org/10.1021/acsaami.1c05720>.
- [69] M.G. Mohamed, S.Y. Chang, M. Ejaz, M.M. Samy, A.O. Mousa, S.W. Kuo, Design and synthesis of bisulfone-linked two-dimensional conjugated microporous polymers for CO₂ adsorption and energy storage, *Molecules* 28 (2023) 3234, <https://doi.org/10.3390/molecules28073234>.
- [70] S.Y. Chang, A.M. Elewa, M.G. Mohamed, I.M.A. Mekhemer, M.M. Samy, K. Zhang, H.H. Chou, S.W. Kuo, Rational design and synthesis of bifunctional Dibenzo [g, p] chrysene-based conjugated microporous polymers for energy storage and visible light-driven photocatalytic hydrogen evolution, *Mater. Today Chem.* 33 (2023) 101680, <https://doi.org/10.1016/j.mtchem.2023.101680>.
- [71] M. Gora, W. Krzywiec, J. Mieczkowski, E.C.R. Maia, G. Louarn, M. Zagorska, A. Pron, Alternating copolymers of diketopyrrolopyrrole or benzothiadiazole and alkoxy-substituted oligothiophenes: spectroscopic, electrochemical and spectroelectrochemical investigations, *Electrochim. Acta* 144 (2014) 211–220, <https://doi.org/10.1016/j.electacta.2014.07.147>.
- [72] T.H. Weng, M.G. Mohamed, S.U. Sharma, I.M.A. Mekhemer, H.H. Chou, S.W. Kuo, Rationally engineered ultrastable three-dimensional (3D) conjugated microporous polymers containing triptycene, tetraphenylethene, and benzothiadiazole units as exceptional high-performance organic electrodes for supercapacitors, *ACS Appl. Energy Mater.* 6 (2023) 9012–9024, <https://doi.org/10.1021/acsaem.3c01933>.
- [73] T.C. Parker, D.G. Dan Patel, K. Moudgil, S. Barlow, C. Risko, J.L. Brédas, J. R. Reynolds, S.R. Marder, Heteroannulated acceptors based on benzothiadiazole, *Mater. Horiz.* 2 (2015) 22–36, <https://doi.org/10.1039/C4MH00102H>.
- [74] M.G. Mohamed, T.H. Mansoure, M.M. Samy, Y. Takashi, A.A.K. Mohammed, T. Ahamad, S.M. Alshehri, J. Kim, B.M. Matsagar, K.C.W. Wu, S.W. Kuo, Ultrastable conjugated microporous polymers containing benzobisthiadiazole and pyrene building blocks for energy storage applications, *Molecules* 27 (2022) 2025, <https://doi.org/10.3390/molecules27062025>.
- [75] B.A.D. Neto, A.A.M. Lapis, E.N. da Silva Júnior, J. Dupont, 2, 1, 3-Benzothiadiazole and derivatives: synthesis, properties, reactions, and applications in light technology of small molecules. *Eur. J. Org. Chem.* 2013 (2013) 228–255, <https://doi.org/10.1002/ejoc.201201161>.
- [76] A.V. Deshpande, U. Kumar, Effect of method of preparation on photophysical properties of Rh-B impregnated sol-gel hosts. *J. Non Cryst. Solids* 306 (2002) 149–159, [https://doi.org/10.1016/S0022-3093\(02\)01054-2](https://doi.org/10.1016/S0022-3093(02)01054-2).
- [77] M.A. Islam, M.A. Chowdhury, M.S.I. Mozumder, M.T. Uddin, Langmuir adsorption kinetics in liquid media: interface reaction model, *ACS Omega* 6 (2021) 14481–14492, <https://doi.org/10.1021/acsomega.1c01449>.
- [78] D.D. Do, *Adsorption Analysis: Equilibria and Kinetics*, Imperial College Press, London, 1998.
- [79] H. Swenson, N.P. Stadie, Langmuir's theory of adsorption: a centennial review, *Langmuir* 35 (2019) 5409–5426, <https://doi.org/10.1021/acs.langmuir.9b00154>.
- [80] F.C. Wu, R.L. Tseng, S.C. Huang, R.S. Juang, Characteristics of pseudo-second-order kinetic model for liquid-phase adsorption: a mini-review, *Chem. Eng. J.* 151 (2009) 1–9, <https://doi.org/10.1016/j.cej.2009.02.024>.
- [81] M.R. Mahmoud, G.M. Rashad, A.M. Elewa, E. Metwally, E.A. Saad, Optimization of adsorption parameters for removal of ¹⁵²⁺¹⁵⁴Eu(III) from aqueous solutions by using Zn-Cu-Ni ternary mixed oxide, *J. Mol. Liq.* 291 (2019) 111257, <https://doi.org/10.1016/j.molliq.2019.111257>.
- [82] G.M. Rashad, M.R. Mahmoud, A.M. Elewa, E. Metwally, E.A. Saad, Removal of radiocobalt from aqueous solutions by adsorption onto low-cost adsorbents, *J. Radioanal. Nucl. Chem.* 309 (2016) 1065–1076, <https://doi.org/10.1007/s10967-016-4726-4>.